

The Effect of Equatorial Noise on the Proton Density Structure of the Inner Van Allen Belt

J. Joseph¹, A. N. Jaynes¹, G. G. Howes¹, M. E. Usanova² and D. P. Hartley¹

¹Department of Physics and Astronomy, University of Iowa, Iowa City, IA, USA.

²Laboratory for Atmospheric and Space Physics, University of Colorado Boulder, Boulder, Colorado, USA.

Corresponding author: J. Joseph (jayasri-joseph@uiowa.edu)

Key Points:

- Observations of wave damping due to finite Larmor radius effect in the inner belt region
- Evidence of wave-particle interaction modifying the proton density profile at L~1.8

Abstract

We present evidence of damping of equatorial noise due to finite-Larmor-radius (FLR) effect in the inner Van Allen belt. Detailed observations of the FLR phenomenon in the inner belt region have not been reported until now. Waves primarily damped by the FLR mechanism can influence the energy dependent proton density structure. We analyze a typical case recorded by the Van Allen probe that involves FLR damping of equatorial noise, which was propagating radially towards the Earth, at L-shell ~ 1.7 . As a result of this damping, protons in the energy range of $\sim 18 - 24$ MeV at L-shell $1.7 < L < 2$ get energized. This kind of wave-particle interaction should be included in the future models of the inner Van Allen belt. The unknown proton loss mechanism reported in Selesnick and Albert (2019) could be an indirect effect of this energy dependent reorganization of protons in the inner belt.

1 Introduction

The inner Van Allen Belt typically extends from an altitude of 1000 km to 12000 km ($1 < L < 3$) above the Earth. This belt primarily consists of highly energetic protons with energies ranging from tens of MeV to hundreds of MeV and electrons with energies of hundreds of keV. These charged particles are trapped by the Earth's relatively strong magnetic fields at low altitude. Protons with energies above 50 MeV in the lower belt are the result of the beta-decay of neutrons created by cosmic ray collisions with nuclei of the upper atmosphere (Dragt et al., 1966; Selesnick et al., 2007; Singer, 1958). Inward diffusion of solar protons during medium to strong geomagnetic storms is the source of the lower energy protons (Hudson et al., 1995; Looper et al., 2005; Lorentzen et al., 2002). The first realistic proton flux maps of near-Earth space using the Proton Telescope (PROTEL) detector on Combined Release and Radiation Effects Satellite (CRRES) was reported by Gussenhoven et al. (1993). The major finding in the CRRES maps was that there appeared to be two quite distinct regions in the inner magnetosphere which are populated by high energy protons – a stable inner region at L-values below 1.8, and a

solar activity-dependent, variable outer region. Selesnick et al. (2018) developed an empirical model of the proton radiation belt from data taken during 2013–2017 by Van Allen Probes satellites. From long-term measurements and simulations Li et al. (2020) have shown that there are no obvious solar cycle variations at $L > 1.2$ for protons (>36 MeV) mirroring near the magnetic equator.

The instrument suite on the Van Allen probe mission has revealed the proton flux density structure in the equatorial region in detail. Measurements of inner radiation belt protons have been made by the Relativistic Electron-Proton Telescopes (REPT) as a function of kinetic energy (21–102 MeV), during September 2012 to September 2019. A sparsely populated region at $L \sim 1.8$ for protons with energy ~ 21 MeV can be seen in the top panel of Figure 1. The strength of the flux density variation reduces with an increase in proton energy (Figure 1 bottom panel). It is surprising to see that the inner belt, which is not easily affected by solar activity, has a semi-permanent nonuniform flux density structure. Based on observations during October 2013 to March 2014, Selesnick et al. (2014) suggested that low solar activity prior to 2012 could contribute to non-uniform flux density. They pointed out that the low-energy main peak in the proton distribution was formed by inward diffusion of injected solar protons over many years. The secondary peak is caused by more recent solar proton injections that have not yet diffused inward to reach the main peak. This double peak structure is most prominent for protons with energies around 21 MeV during 2012 to 2014. Scarcity of protons with energies around 21 MeV at $L \sim 1.8$ could involve additional underlying causes. However, as the solar activity increased, the strong diffusion of solar protons masked the effect of the weak proton removal phenomenon. An updated model simulation by Selesnick et al. (2019) shows that most changes can generally be understood as resulting from effects of radial diffusion combined with steady loss. They have considered the effects of loss due to various mechanism like increased neutral density, elastic Coulomb scattering, plasma wave pitch angle scattering, field-line curvature scattering, and collision with orbital debris. However, these mechanisms could not fully explain the observed losses in the inner belt structure. They expect another, unknown loss mechanism, which is responsible for the energy-dependent proton decay.

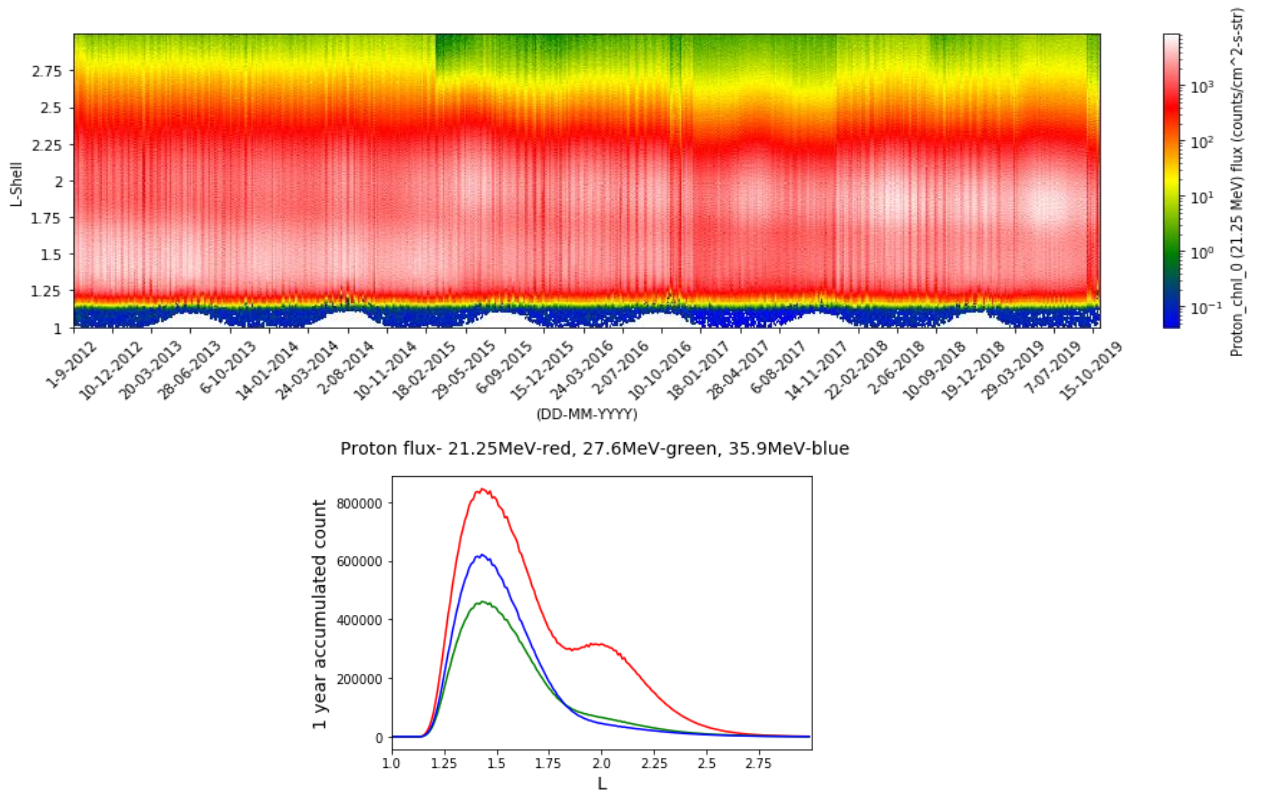


Figure 1. Seven years of (~ 21.25 MeV) proton flux variation with L-shell and time (top panel). Comparative proton flux variations with energies ~ 21.25 MeV (red), ~ 27.6 MeV (green) and ~ 35.9 MeV (blue) (bottom panel) for one year (2013-2014).

In this article, we examine how wave-particle interactions in the inner belt region could play a part in the observed anomaly of ~ 21 MeV protons at $L \sim 1.8$. Particle interactions with different plasma waves can accelerate charged particles and/or drive pitch angle scattering. However, many of the waves which can be observed in the inner belt region (e.g., EMIC, plasmaspheric hiss, etc.) primarily interact with radiation belt electrons and/or lower energy ring current ions, and are unable to affect protons with high (\sim MeV) energies. In this study, we concentrate on the wave particle interaction of perpendicular propagating equatorial noise, which is abundant in the low latitude region of the inner belt.

Equatorial noise is electromagnetic waves observed in the equatorial region of the inner magnetosphere at frequencies between the proton-cyclotron frequency and the lower hybrid frequency. As early as 1970, Russell et al. (1970) noticed the electromagnetic noise near the magnetic equator. Since then, they are rather routinely observed at radial distances between about 2 to 5 Earth radii (R_E) and within about 5° from the geomagnetic equator (Santolík et al., 2004; Nemec et al., 2005; Ma et al., 2013; Hrbáčková et al., 2015). These waves propagate perpendicular to Earth's magnetic field. Gurnett (1976) first suggested that these waves could interact with energetic protons, alpha-particles, and other energetic ions near the magnetic equator. Basic propagation properties of these waves were theoretically analyzed by Russell et al. (1970). These waves can be classified as fast magnetosonic waves propagating in the perpendicular direction to Earth's magnetic field. Propagation properties were verified by Santolík et al. (2002) using Cluster data. They show that these waves are likely to have been generated by instability of ion distributions at a distant region and propagate with a significant radial component. Horne et al. (2011) suggested that the fast magnetosonic mode can cause large diffusion of ring current protons in energy and to a lesser extent in pitch angle. A global distribution and empirical models of fast magnetosonic waves is presented in Ma et al. (2019). In this article, we examine the role of equatorial noise in selectively removing protons with energy around 21 MeV from L-shells around 1.8.

2 Instrumentation

The Van Allen Probes (A and B) were two identical spacecraft with highly elliptical orbits close to the equatorial plane. Orbital period of these spacecraft was approximately nine hours during which they traversed through both inner and outer Van Allen radiation belts. For this study, we used magnetic and electric field data as well as information about proton flux densities recorded by probe-A.

The Electric and Magnetic Field Instrument Suite and Integrated Science (EMFISIS) (Kletzing et al., 2013) fluxgate magnetometer (MAG) recorded continuous time domain data with a sampling frequency of 64 Hz. As we are interested in waves in the frequency range of 20 to 30 Hz and their harmonics, this time domain data does not satisfy our requirement. Here we use the onboard waveform frequency receiver (WFR) of EMFISIS instrument for spectral data. In the survey

mode, every six seconds, the WFR captures waveforms of electric and magnetic fields for a duration of ~0.5 second. Combinations of three electric and three magnetic field components are used to compute a 6x6 power spectral matrix. These matrices are available at 65 quasi-logarithmically spaced frequencies ranging from 2 Hz to 11 kHz, at a cadence of six seconds.

To obtain background cold plasma densities, the upper hybrid method (UHR) is widely used. In general, total electron density in a plasma can be derived from the EMFISIS UHR frequency $w_{uh}^2 = w_{ce}^2 + w_{pe}^2$ measurements, which depend on the electron cyclotron frequency $w_{ce} = \frac{eB}{m}$ and the plasma frequency $w_{pe} = \sqrt{n_e e^2 / (\epsilon_0 m)}$, where e and m are the charge and the mass of electron, n_e is the cold plasma density, B is the background magnetic field and ϵ_0 is the free space permittivity. However, for low L (~1.7) region, w_{ce} is of the order of ~170 kHz and falls beyond the instrument's range. Total plasma density can also be estimated from the spacecraft potential for the positive spacecraft charging. This technique is used by the Electric Field and Waves Instrument (EFW) (Wygant et al., 2013) to determine the cold plasma density. In this study, we use data from EFW as well as estimation from plasmaspheric hiss for background cold plasma densities. The plasma density may be estimated from plasmaspheric hiss through $B^2 = \frac{1}{c^2} \left(1 - \frac{\omega_{pe}^2}{\omega(\omega - \omega_{ce})} \right) E^2$, where c is the speed of light, E^2 and B^2 are the electric and magnetic field wave power respectively at angular wave frequency, ω , under the assumption of parallel wave propagation. The plasma density is determined from ω_{pe} before applying a statistical calibration based on the UHR method (Hartley et al., 2018).

The Relativistic Electron Proton Telescope (REPT) (Baker et al., 2013) proton flux measurements are used to look at the dynamics of the inner belt proton population. REPT uses silicon particle detectors in a particle telescope configuration to measure the electron and the proton flux in energy range of 1–20 MeV and 17–200 MeV, respectively. Proton energy bins represented as channel 0-6 are centered around 21.25 MeV, 27.60 MeV, 35.90 MeV, 46.70 MeV,

60.70 MeV, 78.90 MeV, and 102.60 MeV, respectively. Channel-7 represents the integral flux of protons with energies above channel-6 and up to 200 MeV.

3 Observations

We examine data from Van Allen probe-A during its 970 transits through $L < 3$ during March 1st, 2013 to February 28th, 2014. We analyze the six diagonal components of the power spectral density matrix namely EuEu, EvEv, EwEw, BuBu, BvBv and BwBw for electric and magnetic fields recorded by EMFISIS WFR. These observations are in instrument's 'u-v-w' coordinates, where the 'u' and 'v' components are directed along the two long spin plane antennas, and the 'w' component is directed along the short spin axis antenna. The spin axis (w) is generally pointed in the direction of the sun. Differential flux of protons at different energies are obtained from REPT spin averaged energy bins namely FPSA 0-7.

3.1 Events

From the WFR power-frequency spectrograms we have identified clear structures of spectral lines in the frequency range of tens of Hertz within $1.5 < L < 3.0$ in 25% of transits through the inner belt. All of them show similar harmonic structures which is consistent with properties of equatorial noise. Approximately 5 - 10% of these equatorial noise observations reveal an unexpected damping phenomena, where all the harmonics of the waves are attenuated simultaneously, and the damping location does not match the profile of any local cyclotron frequency. We perform a detailed analysis of one of these wave damping events, which was recorded during the outbound section of the inner belt transit on 29th June 2013 between 01:30 and 02:40 UT.

Figures 2, a-f, show frequency-time spectrograms of the three components of the electric and magnetic fields for the event. Because of the highly eccentric equatorial orbit of Van Allen Probes and their quick transit through the inner belt region, the spacecrafts occasionally captured the whole life cycle of the confined noise in the magnetic equatorial plane. Spectrograms in Figure 2 show a harmonic structure with a frequency spacing of about 20 Hz. The vertical dotted lines on the spectrograms indicate the location of damping of the harmonic structure.

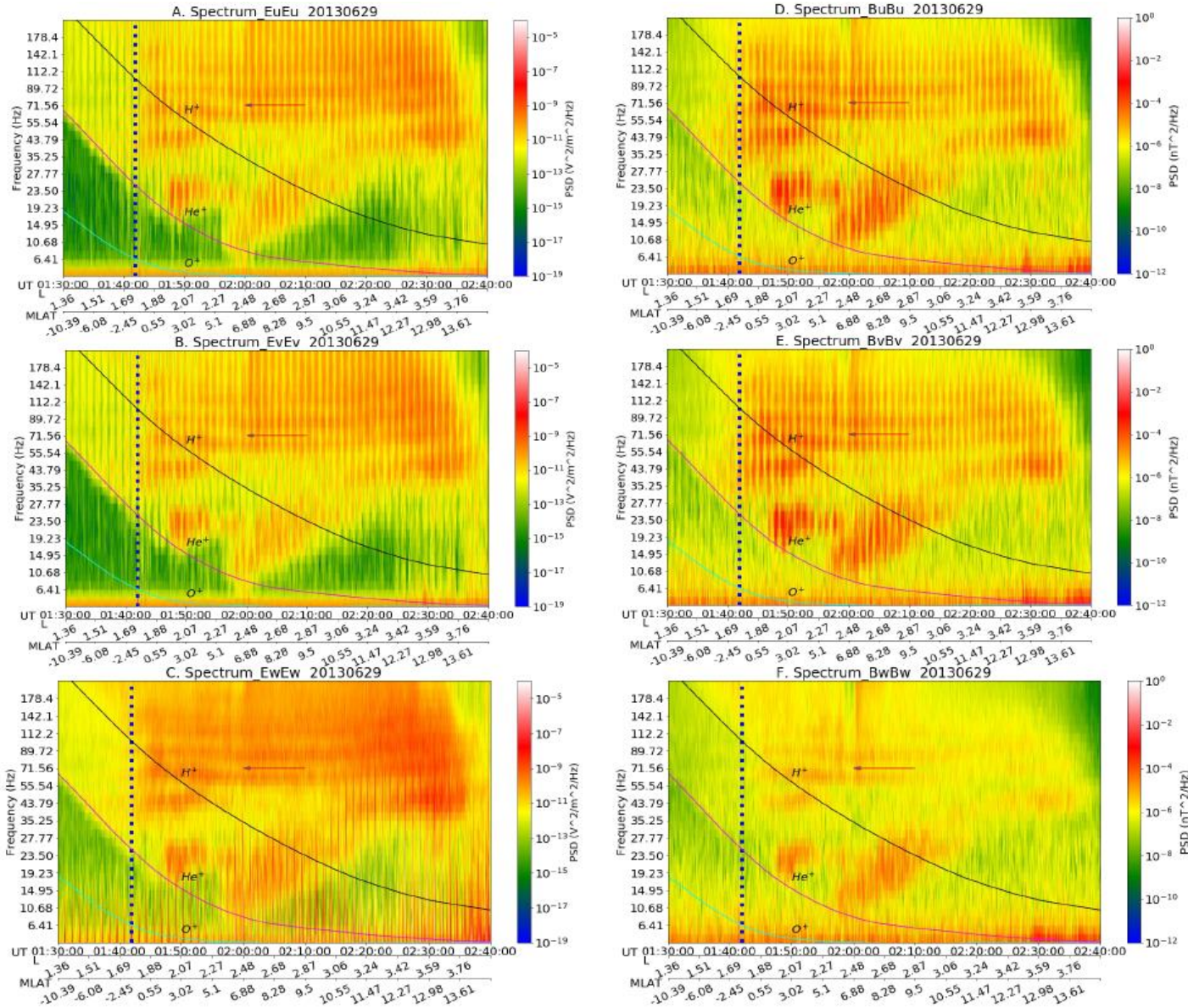


Figure 2. Electric and magnetic power spectral density during the events of 29th June 2013.

Black, magenta, and cyan curves correspond to H^+ , He^+ and O^+ cyclotron frequencies, respectively. Direction of the wave propagation is shown by the arrow and the location at which significant wave attenuation/damping occurs is shown by the vertical dotted line.

3.2 Wave properties

The wave propagation parameters are determined using the singular value decomposition (SVD) method (Santolík et al., 2003). Figure 3, a-f show the Poynting flux parameters (magnitude and polar angle), wave ellipticity, wave normal angle and the orientation of the wave electric vector

around the event. The coordinate system used here is field-aligned, with axis-3 (z) along the background magnetic field (B_0), axis-1 (x) pointing outward from the Earth and axis-2 (y) pointing eastward. The wave is predominantly linearly polarized (\sim zero ellipticity) and propagates almost perpendicular to the background magnetic field as shown by the wave normal angle. The wave Poynting flux is also mostly perpendicular with respect to the background magnetic field. The fundamental frequency of these waves can be determined by the frequency spacing of the harmonics (Boardsen et al., 1992). This fundamental frequency corresponds to the proton cyclotron frequency of the generation region (Gurnett, 1976). Thus, we can conclude the wave with 20 Hz frequency spacing have been generated at around $L \sim 2.8$ and propagated inwards to $L \sim 1.75$. It is to be noted that there was also an outward propagating branch of the wave, which traveled from $L \sim 2.8$ to $L \sim 3.7$. In this study, we focus on the Earthward propagating arm of the wave.

The dispersion relation of magnetosonic waves can be derived from the system of ideal magnetohydrodynamics (MHD) equations (Cairns, 1985)

$$\omega = kv_{\pm} = k\sqrt{\frac{1}{2}\left[v_A^2 + v_S^2 \pm \sqrt{(v_A^2 + v_S^2)^2 - 4(v_A v_S \cos \theta)^2}\right]},$$

where the wave speed (v) of the fast mode corresponds to the '+' sign and the slow mode to the '-' sign. The dispersion relation of fast magnetosonic mode is relevant in our case. Here v_A is the Alfvén speed, v_S is the sound speed, k is the magnitude of the wave vector and θ is the angle between the wave vector and the background magnetic field. For waves perpendicular to the background magnetic field ($\theta \sim 90^\circ$), the dispersion relation reduces to

$$\omega = k\sqrt{v_A^2 + v_S^2}$$

Sound speed can be approximated in terms of plasma parameters using equation $v_S^2 = \beta v_A^2$, where β is ratio of the plasma pressure to the magnetic pressure. For our observation, we found $\beta \sim 0.1$ at $L \sim 1.7$.

In the limit of low β plasma and perpendicular wave propagation ($\theta \sim 90^\circ$), at low L (< 2), the dispersion equation for low ($\lesssim 10$) harmonic (Horne et al., 2000) magnetosonic waves can be further approximated as

$$199 \quad \omega \sim kv_A \quad (1)$$

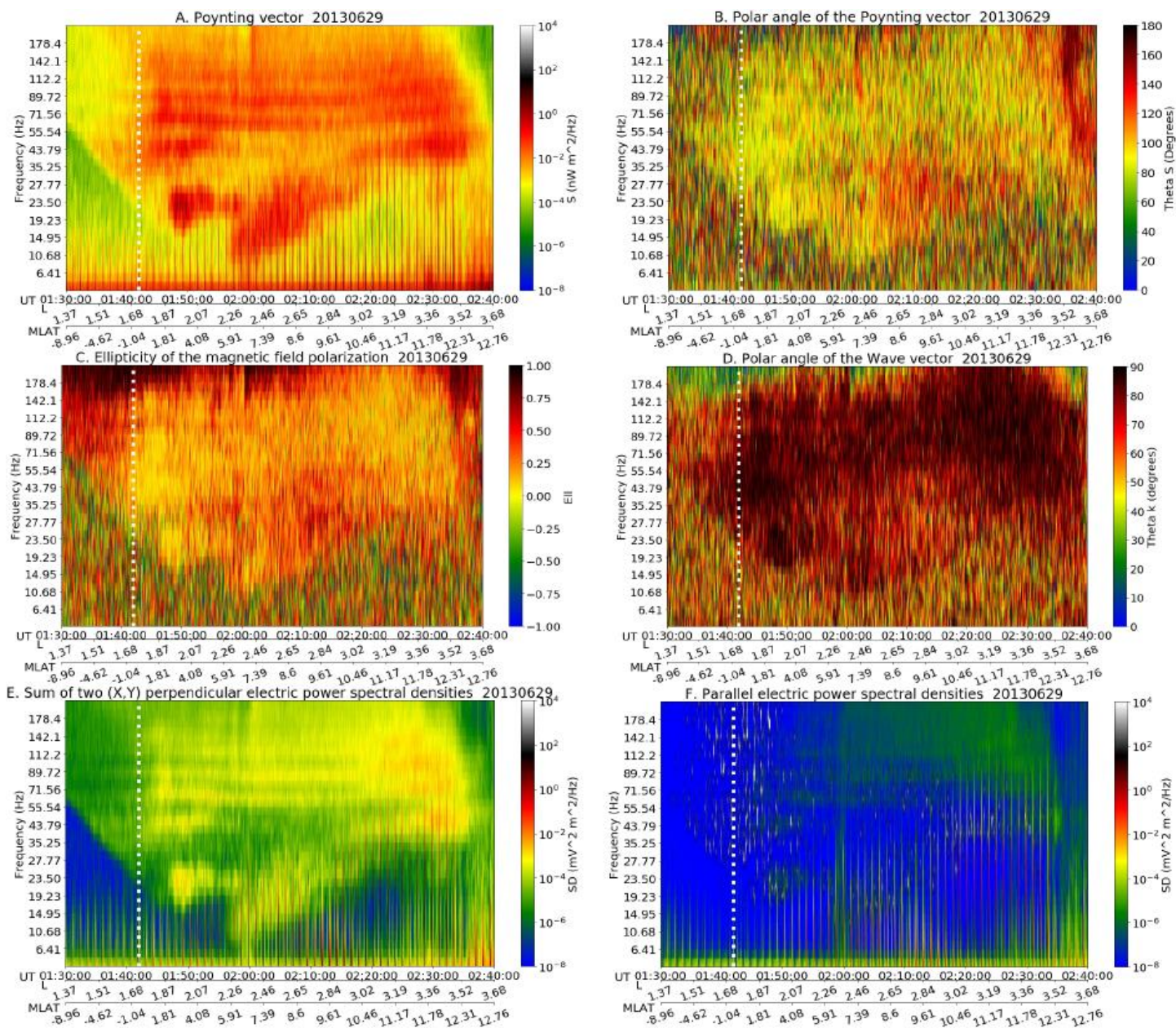


Figure 3. A. Flux and B. polar angle of the Poynting vector, C. Ellipticity and D. wave normal angle of the wave, E. Perpendicular and F. parallel components of the electric vector of the wave for the event on the 29th of June, 2013.

4 Analysis and discussion

We perform a detailed analysis of the unusual damping of the equatorial noise on the 29th June, 2013. The two types of damping (Somov, 2013) that are commonly encountered in collisionless magnetized plasma are Landau / transit time damping given by equation

$$\omega - k_{\parallel} v_{\parallel} = 0$$

and cyclotron harmonic damping given by (non-relativistic) equation

$\omega - k_{\parallel} v_{\parallel} - n\omega_c = 0$, where ω is the wave frequency, k_{\parallel} is the parallel wave number, n is an integer and v_{\parallel} and ω_c are the parallel velocity and cyclotron frequency of the charged particle, respectively. All directions referred here are with respect to the background magnetic field. The non-relativistic forms of the damping equations are a good approximation as the energy range of the protons in our study is much smaller (<24 MeV) compared to the rest energy (938 MeV) of the proton.

In our case of predominantly perpendicular wave, which propagated over ~7000 km without any significant damping, $k_{\parallel} \sim 0$. To estimate the effect of any Landau damping due to bulk plasma, we assume the angle of propagation to be close to 90°. The theoretical analysis of the expected damping rates due to plasma condition at $L=1.75$ are described in section 4.1.

4.1 Theoretical analysis

We carried out a theoretical analysis for the 20 Hz harmonic wave propagating through plasma and its damping at $L \sim 1.75$ for the event of 29th June 2013. In the Appendix, we show that the effect of the inhomogeneous plasma conditions on the nearly perpendicular waves of approximately 20 Hz and higher harmonic frequencies is to refract the waves away from the perpendicular direction of propagation. The first five harmonic modes, presumed to be generated by the ion Bernstein instability (Gary et al., 2010), are generated around $L \sim 2.8$. The Poynting flux of these waves propagated radially inward down to $L = 1.75$, where the waves appear to suffer a sudden onset of strong damping (Figure 3A). The propagation of waves in an inhomogeneous plasma is governed by the ray equations (A1) (Weinberg, 1962). As detailed in the Appendix, the frequency of the waves ω remains constant as the waves propagate radially inward, consistent with the observations in Figure 2. Our analysis predicts that the parallel wavenumber k_{\parallel} also remains constant. The perpendicular wavenumber (k_{\perp}) on the other hand, decreases in the inhomogeneous plasma conditions. Here we use the normalized values of the wavenumber kd_i , where d_i is the ion inertial length (see Appendix). These normalized values map from $0.8 \leq k_{\perp} d_i \leq 2.9$ for the first five ion Bernstein modes at $L = 2.8$ down to values $0.3 \leq$

$k_{\perp} d_i \leq 1.1$ at $L = 1.75$, decreasing by a factor of approximately 2.6. This decrease in $k_{\perp} d_i$, along with the increase in the local ion cyclotron frequency Ω_i , shifts these waves from the regime of ion Bernstein modes (at harmonics of the local ion cyclotron frequency) to that of the fast magnetosonic wave, as shown by the green dots in Figure A2. The decrease of k_{\perp} with constant k_{\parallel} also leads to a decrease in the angle of propagation relative to the magnetic field, $\theta = \tan^{-1} \left(\frac{k_{\perp}}{k_{\parallel}} \right)$, effectively refracting the waves away from nearly perpendicular propagation. Below we assess how this refraction, along with the presence of a significant population of energetic protons (a few percent relative density), may lead to the sudden onset of damping of these waves at $L = 1.75$.

In Figure 4, we use the PLUME Vlasov-Maxwell linear dispersion relation solver (Klein and Howes, 2015) to plot the frequency normalized to the local ion cyclotron frequency (ω/Ω_i) in panel-a and the normalized damping rate ($-\gamma/\omega$) in panel-b as a function of the perpendicular wavenumber $k_{\perp} d_i$ for the plasma conditions (ion plasma beta, $\beta_i = 0.173$, ratio of ion temperature to electron temperature, $T_i/T_e = 1$, ratio of ion thermal velocity to speed of light, $v_{ti}/c = 3.3 \times 10^{-3}$) at $L = 1.75$, ignoring the presence of any energetic protons. We take the parallel wavenumber to be $k_{\parallel} d_i = 10^{-2}$ in these calculations, satisfying the nearly perpendicular limit $k_{\parallel} \ll k_{\perp}$. The Hall MHD dispersion relation for the fast magnetosonic wave, in the limit of nearly perpendicular propagation $k_{\parallel} \ll k_{\perp}$ and small parallel wavenumber $k_{\parallel} d_i \ll 1$, given by equation A2, is also plotted (red dashed) in panel-a of figure 4 for comparison. At $\omega = \Omega_i$, the Vlasov-Maxwell solution (blue) shows that the ion Bernstein mode undergoes a mode conversion to the fast magnetosonic wave, arising from physical effects excluded from the fluid theory of Hall MHD (red dashed). Note that in the absence of any energetic proton population, the damping rate (black) in panel-b is very low for the expected perpendicular wavenumber range of the five harmonic modes, $0.3 \leq k_{\perp} d_i \leq 1.1$ at $L = 1.75$. Therefore, in the absence of other effects, the damping of these fast magnetosonic waves under the plasma conditions at $L = 1.75$, with an estimated proton thermal energy of 5 keV, is expected to be weak.

To explore how the presence of a population of energetic protons impacts the damping of these fast magnetosonic waves, we included a small population of 21 MeV protons to emulate the 21 MeV REPT channel (18.5-24 MeV) in our PLUME calculations. The composite damping effect is presented in the panel-b of Figure 4 for an energetic to core proton percentage of $n_{ep}/n_p =$

0.01% (blue short dashed), 0.1% (blue dotted), 1% (blue long dashed), and 3% (blue solid). Energetic protons increased the damping rate by many orders of magnitude, particularly in the range $0.5 \leq k_{\perp} d_i \leq 0.9$. Therefore, the presence of an energetic proton population in the inner radiation belt can significantly enhance the damping of these fast magnetosonic waves at $L \sim 1.75$. For a clear understanding of the collisionless damping at $L \sim 1.75$, it is necessary to separate the damping contributions from each species. Here we use PLUME solver to evaluate the contributions due to the Landau/transit-time damping and the cyclotron resonance ($n=1$) damping caused by different species, namely the core electrons, the core protons and the energetic (18.5-24 MeV) protons. In Figure 4c, we consolidate all the damping contributions including the contribution from the (3%) 21 MeV energetic protons. As seen from Figure 4c, at $k_{\perp} d_i < 0.4$, Landau damping by the core 5 kV electrons and transit-time damping by the 21 MeV protons dominate the overall damping, with nearly equal contribution. Also, at $k_{\perp} d_i > 1$, the damping is dominated by the $n=1$ cyclotron resonance with the core 5 keV protons. However, in the range $0.5 < k_{\perp} d_i < 0.9$, which is most relevant for the fast magnetosonic waves under investigation here, we find that the damping is dominated by the $n = 1$ cyclotron resonance with the 21 MeV protons.

The effects of wave refraction can also significantly enhance the damping of the 20 Hz and higher harmonic waves. In Figure 4d, we plot the normalized damping rate $-\gamma/\omega$ vs. the angle of propagation θ for the fast magnetosonic wave with $kd_i = 0.3$ ($n = 1$ mode, black dotted) and $kd_i = 1.1$ ($n = 1$ mode, black dashed) with $n_{ep}/n_p = 0\%$. Note that the damping rate drops off precipitously for $\theta \geq 88^\circ$, meaning that the waves are essentially undamped at nearly perpendicular propagation, but that a slight refraction towards the parallel direction (by even as little as 1°) can lead to a dramatic increase in the damping rate. For example, if the normalized perpendicular wavenumber decreases by a factor of 2.6 and the normalized parallel wavenumber decreases by a factor of 1.5, then a net decrease of k_{\perp}/k_{\parallel} by a factor 1.73 is expected (see Appendix). For $n_{ep}/n_p = 0\%$, a wave with an initial angle $\theta = 89^\circ$ at $L = 2.8$ would be refracted to an angle $\theta = 88.3^\circ$ at $L = 1.75$, leading to an increase in the damping rate of more than three orders of magnitude. The presence of $n_{ep}/n_p = 3\%$ energetic protons for $kd_i = 0.3$ (blue dots) serves to increase the damping rate but does not change the qualitative finding of dramatic increases in the damping rate with a slight refraction away from perpendicular propagation.

297 In summary, it appears likely that the sudden damping of the 20 Hz and its higher harmonic
298 waves at $L = 1.75$ is caused by a combination of the two effects – one being the presence of a
299 small percentages of 18.5-24 MeV protons and the other being the wave refracting away from
300 the perpendicular direction. For $n_{ep}/n_p = 3\%$, the damping rate peaks at about $-\gamma/\omega = 0.05$.
301 With this damping rate, half of the wave amplitude (or three quarters of the wave energy) is
302 damped within approximately two perpendicular wavelengths, enabling a sudden onset of the
303 damping. For the 20 Hz mode with $k_{\perp}d_i = 0.3$ and $d_i = 4.6$ km at $L = 1.75$, we obtain a
304 perpendicular wavelength of $\lambda_{\perp} = 96$ km, so the wave is expected to be damped out over a
305 distance of a few hundred kilometers, providing a viable explanation for the sudden damping of
306 all five harmonics of the fast magnetosonic waves at $L \sim 1.75$.

307

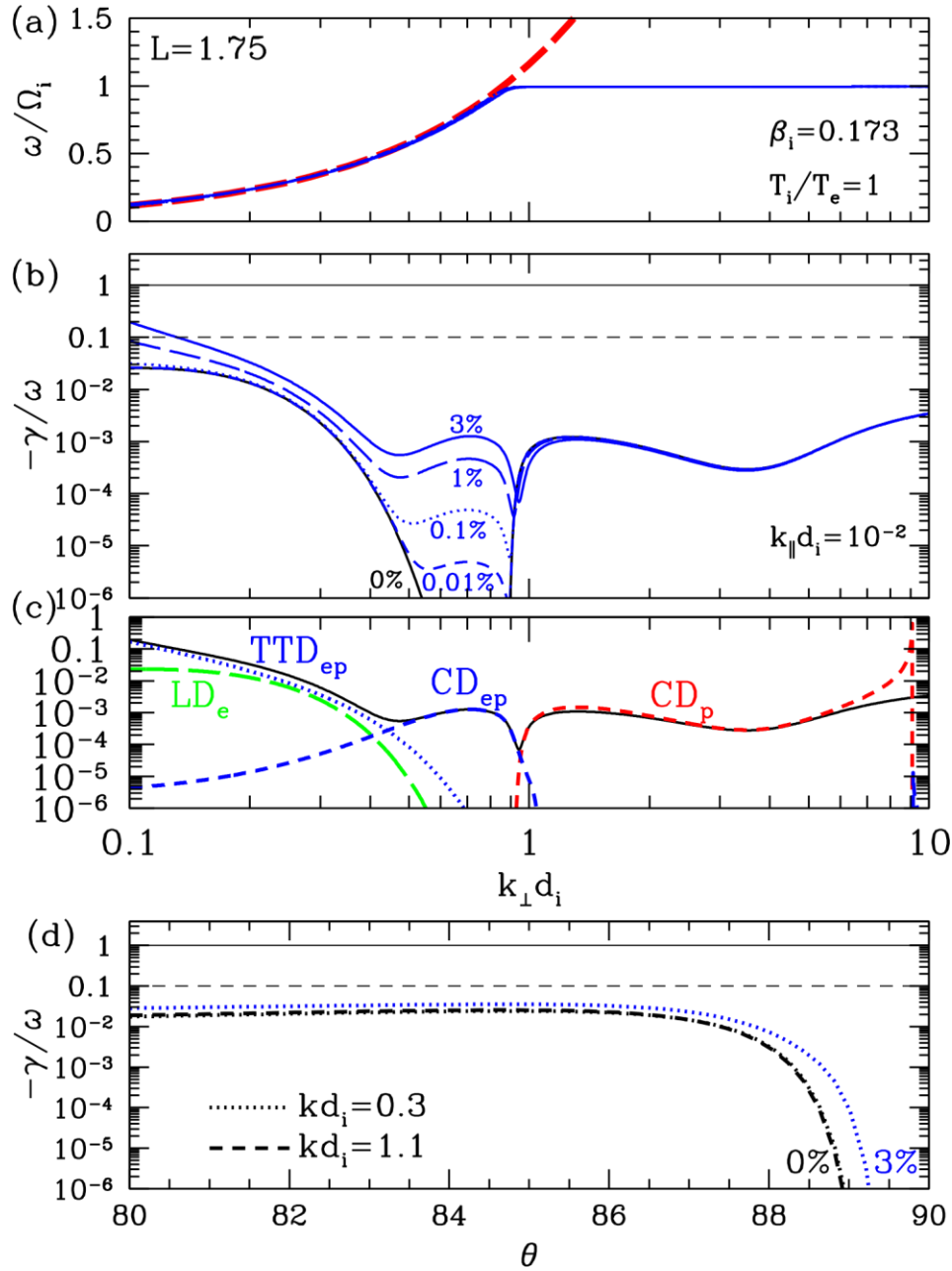


Figure 4. (a) normalized real frequency ω/Ω_i (blue) along with the Hall MHD linear dispersion relation for fast magnetosonic waves (red dashed) versus normalized perpendicular wavenumber $k_{\perp} d_i$. (b) normalized damping rate $-\gamma/\omega$ versus normalized perpendicular wavenumber $k_{\perp} d_i$ for different percentages of 21 MeV protons (blue curves). Damping rate without any energetic proton is also shown (black). (c) various damping contributions from different species for the $n_{ep}/n_p = 3\%$ case versus normalized perpendicular wavenumber $k_{\perp} d_i$. Contributions from $n=1$ cyclotron damping by the core 5 keV protons (red dashed), Landau damping by the core 5 keV electrons (green long dashed), transit-time damping by the 21 MeV protons (blue dotted), and $n=$

1 cyclotron damping by the 21 MeV protons (blue dashed) are shown. (d) the normalized damping rate $-\gamma/\omega$ versus the angle of propagation θ for the fast magnetosonic wave with $kd_i=0.3$ (black dotted) and $kd_i=1.1$ (black dashed) without any energetic proton. Effect of the presence of 3% energetic proton with $kd_i=0.3$ (blue dotted) is also shown.

4.2 Discussion

From the theoretical analysis it is clear that ~21 MeV protons at $L \sim 1.75$ have an important role to play in our case of wave damping. The physical mechanism of the subtle damping effect needs explanation. As Larmor radius of ions with certain energy approaches the perpendicular wavelength of the waves propagating in the plasma, we observe a wave particle interaction due to finite Larmor radius (FLR) effect (Stix, 1990). FLR effects depend on the ratio R/L , where R is the Larmor radius and L is the spatial scale of field/plasma inhomogeneity (Stasiewicz, 1993). This phenomenon introduces a significant correction to the ideal MHD condition, which assumes particles gyro-radius to be much smaller than the wavelength. For theoretical studies, FLR effects are implicitly included in the kinetic Vlasov formulations and electromagnetic particle simulation codes. FLR effect and cyclotron harmonic effect are closely related. FLR wave particle interaction requires the resonant condition $k_{\perp}v_{\perp} \geq n\omega_c$ (Stix, 1990), where k_{\perp} is the perpendicular wave number, ω_c and v_{\perp} are the cyclotron frequency and the perpendicular velocity of the charged particle. By substituting $v_{\perp} = \omega_c r_L$, where r_L is the Larmor radius of high energy protons, we get $k_{\perp}r_L \geq n$. To estimate the significance of the FLR effect due to ~21 MeV protons, we calculate r_L and λ_{\perp} for our observation.

Since $k_{\perp} \sim k$, from equation 1, $\omega \sim k_{\perp}v_A$.

$$\lambda_{\perp} = \frac{2\pi}{k_{\perp}} \approx \frac{v_A}{f} = \frac{B_0/\sqrt{\mu_0 n_0 m_i}}{f} \quad (2),$$

Where f is the frequency of the wave in hertz, v_A is the Alfvén velocity, B_0 is the background magnetic field, μ_0 is the free space permeability, n_0 is the plasma density and m_i is the mass of ion. Wavelengths (λ_{\perp}) for equatorial noise with 20 Hz frequency at various L-shells are calculated from equation-2.

The gyro-radius of protons at the equatorial plane are calculated by:

$$r_L = \frac{1}{2\pi f_{cp}} \sqrt{\frac{2E}{m_p}} \quad (3),$$

where E is the energy of the proton; f_{cp} and m_p are the cyclotron frequency and the mass of the proton, respectively.

To determine the region of effective FLR wave particle interaction, we plot (Figure 5) the perpendicular wavelength (λ_{\perp}) of the 20 Hz wave and the Larmor radius (r_L) of 21 MeV and 27 MeV protons with respect to L-shell. The shaded region shows the L-shell values, where the Larmor radius of 21 MeV proton is approximately equal to the wavelength. We can clearly see that around $L \sim 1.8$, 21 MeV proton can interact with $n \cdot 20$ Hz waves. Theoretical estimate of the damping rate due to presence of small ($< 3\%$) amount of 18.5-24.0 MeV (referred as 21 MeV) proton around $L \sim 1.7$ is shown in Figure 4b. Flux density of 18.5-24.0 MeV proton at $L \sim 1.7$ is estimated to be ~ 1 -2% by NASA's AP-8 radiation belt model (Vette, 1966; Sawyer and Vette, 1976). For a perpendicularly propagating waves with the wave magnetic field parallel and the wave electric field perpendicular to the static magnetic field, wave-particle interactions modify the energy of the ions rather than cause pitch angle scattering (Gurnett, 1976). Figure 3. Panel e and f confirms that the direction of the wave electric field vector is perpendicular. The FLR interaction results in an energy exchange process, where the $n \cdot 20$ Hz wave loses its energy, and ~ 21 MeV protons gain energy and shift to higher energy level. This phenomenon would lead to a reduction in the number of observed ~ 21 MeV proton around $L \sim 1.75$. This is consistent with the observation of paucity of ~ 21 MeV protons at $L \sim 1.75$ in Figure 1.

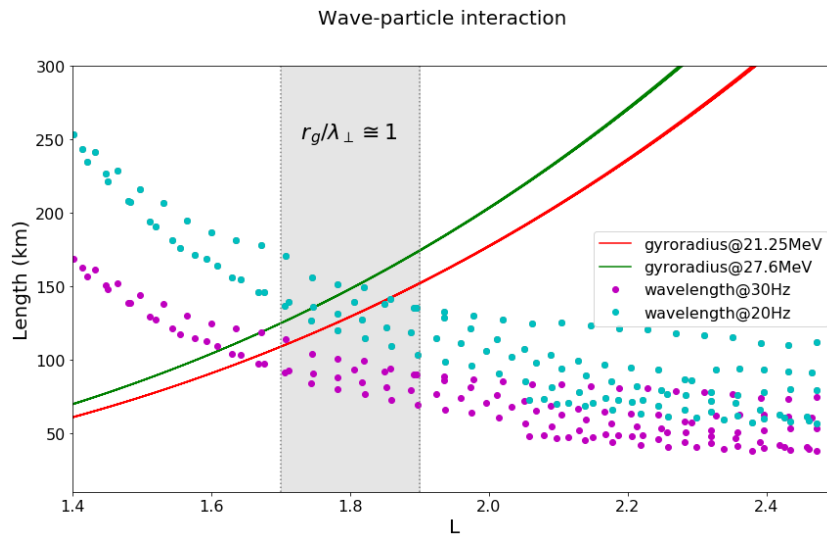


Figure 5. Gyro-radii and wavelengths versus L-shell. Shaded region represents the L-shell domain of expected proton energization.

For the event on 29th June 2013, the overall damping at $L \sim 1.75$ is a combination of FLR effect caused by 18.5-24.0 MeV protons and Landau damping by the thermal electrons. A detailed examination of especially Figure 2, panel C and Figure 3 panel E, reveals that the wave was damped in two stages. The first stage damping was encountered at $L \sim 1.75$, where all the harmonics of the wave was attenuated by ~ 2 orders of magnitude. A second stage cyclotron harmonic damping of the remaining wave energy was observed at He^+ cyclotron frequency as the wave changed to left hand polarization (Figure 3C) and became less oblique (Figure 3D). In this paper for the first time, we report the evidence of FLR interaction of equatorial noise with energetic protons trapped near the magnetic equator at low L . Protons with energies around 21 MeV at $1.7 < L < 1.9$ become energized by equatorial noise. This causes the apparent reduction of the number of 18.5-24.0 MeV protons at $1.7 < L < 1.9$ as they are shifted to higher energies. Thus, presence of this type of equatorial noise plays a crucial role in structuring the inner Van Allen belt proton density profile. This loss mechanism should be included in future models of the inner Van Allen belt. The unknown cause of energy dependent proton loss reported in Selesnick et al. (2019) could be due to the specific wave-particle interactions described here.

5 Conclusions

This paper presents the observation and theoretical analysis of a new mechanism of damping of the equatorial noise at $L < 2$. Previous studies suggest that the waves are cutoff at the frequency slightly above the helium gyrofrequency due to the absorption of helium ions, or the wave power could be converted into left-hand polarized EMIC waves (Horne and Miyoshi, 2016). Here, we show that substantial damping of the wave could also be caused due to the finite Larmor radius effect by a small percentages of high energy (18.5- 24.0 MeV) protons. Moreover, we show that the interaction between the equatorial noise and the energetic protons results in energization of the protons due to the particular orientation of the wave electric field. This energy dependent wave-particle interaction will affect the proton density structure of the inner Van Allen belt.

Appendix

The Van Allen Probes observations of the radial distribution of approximately 20 Hz and higher harmonic waves over the range of radial distances given by $1.75 \lesssim L \lesssim 3.75$ suggests a picture of

radially separated locations of wave generation, propagation, and damping. In particular, we observe in Figure 2 what appears to be a fundamental mode at $f \simeq 20$ Hz and four higher harmonics $n = 2, 3, 4, 5$. Looking at the magnitude of the Poynting flux in Figure 3(A) and the polar angle of the Poynting flux in Figure 3(B), we observe clear trains of waves in the range $1.75 \lesssim L \lesssim 2.8$ propagating approximately radially inward perpendicular to the Earth's dipolar magnetic field.

To illuminate the underlying kinetic plasma physics that is responsible for these wave observations, it is important to examine the profiles of the plasma parameters as a function of the radial distance L . In Figure A1, we plot (a) the magnitude of the magnetic field, (b) the electron density, and (c) the ion plasma beta β_i versus L . In calculating the plasma beta value, we have estimated the ion and electron temperatures to be $T_i = 5$ keV and $T_e = 5$ keV. A key observation in Figure A1(c) is that the value of β_i peaks at approximately $L \simeq 2.9$, suggesting the possibility that a kinetic instability at this radial distance is responsible for generating the waves we observe that propagated inward from this region.

A likely candidate for this instability is the ion Bernstein instability driven by a proton ring distribution with $\partial f_p(v_\perp)/\partial v_\perp > 0$. Gary et al. (2010) explored the detailed linear physics of the ion Bernstein instability, finding that it drives unstable ion Bernstein modes with nearly perpendicular wave vectors, $k_\parallel \ll k_\perp$, and growth rates that peak for plasma β_i values of $0.1 \leq \beta_i \leq 1$. We therefore suggest that it is likely that the waves reported in this paper arise from the ion Bernstein instability driven by a proton ring distribution at $L \sim 2.8$, and these waves then propagate radially inward nearly perpendicular to the magnetic field.

To further explore the properties of the linear kinetic wave modes around $L \sim 2.8$, we numerically solve the Vlasov-Maxwell linear dispersion relation using the PLUME code (Klein and Howes, 2015). We take the plasma parameters to be $\beta_i = 1.19$, $T_i/T_e = 1$, and $v_{ti}/c = 3.3 \times 10^{-3}$. Choosing $k_\parallel d_i = 10^{-2}$, we solve the frequency of the linear wave modes normalized to the local ion cyclotron frequency ω/Ω_i vs. the normalized perpendicular wavenumber $k_\perp d_i$, as shown in Figure A2(a). Here the ion inertial length is given by $d_i = c/\omega_{pi} = v_A/\Omega_i$, where c is the speed of light, ω_{pi} is the ion plasma frequency, v_A is the Alfvén velocity, and $\Omega_i = qB/m_i$ is the (angular) ion cyclotron frequency. The fast magnetosonic wave (black dotted) at $k_\perp d_i < 0.5$ converts to the $n = 1$ Bernstein mode at $k_\perp d_i > 0.5$. The ion Bernstein modes up to $n = 7$ (blue)

show that, for these parameters, there exist frequency gaps over the frequency ranges $(2n+1)/2 \leq \omega/\Omega_i \leq n+1$ for $n = 1, 2, 3, \dots$, consistent with the gaps between the harmonics in Figure 2. Note that, since the group velocity at which a wave propagates in the perpendicular direction is given by $\partial\omega/\partial k_\perp$, the figure shows that each harmonic propagates only over a narrow range of $k_\perp d_i$ where the slope of ω vs. k_\perp is nonzero. We have plotted green dots on Figure A2(a) to be representative of these perpendicularly propagating ion Bernstein harmonic modes. Using linear instability calculations, Gary et al. (2010) show that, for a given choice of parameters, a finite number of harmonic modes are driven unstable, with the growth rates generally decreasing for higher mode number, and with nearly perpendicular angles of propagation over the range $86^\circ \leq \theta \leq 89^\circ$ that increase with the unstable wave mode number. In the analysis below, we focus on first five harmonic modes, $n = 1, 2, 3, 4, 5$.

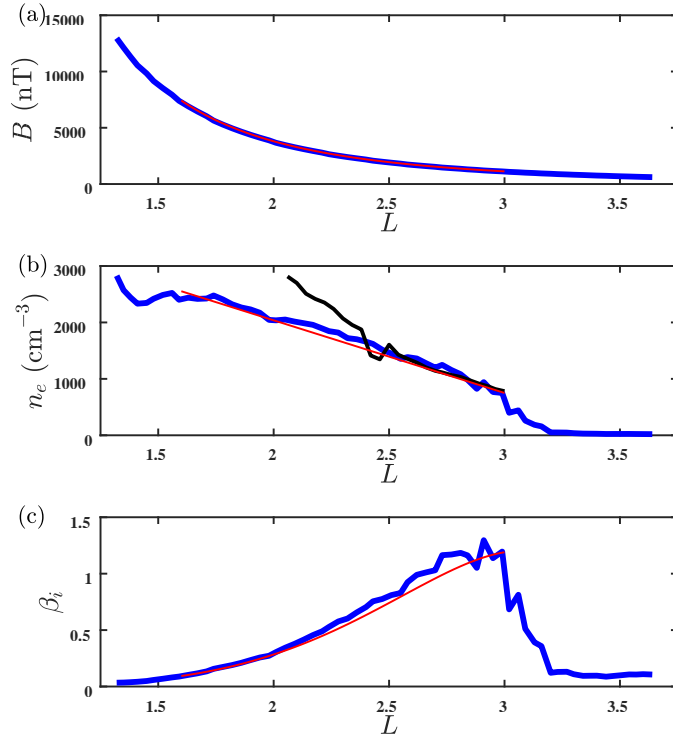


Figure A1. Measured profiles of (a) the magnitude of the magnetic field (blue), (b) the electron density (blue–inbound, black–outbound), and (c) the ion plasma beta β_i versus L (blue), and simple fitted models of these profiles (red) over the range $1.6 \leq L \leq 3$. Note: On the outbound pass of Van Allen Probes from 01:30 to 02:15 during which the event occurred, the electron density information was not available for $L < 2$ (black), so we have substituted the electron density for the previous inbound pass from 00:00 to 01:15 (blue).

To interpret the Van Allen Probes observations of the radial distribution of 20 Hz and higher harmonic waves, we must analyze the propagation of wave modes primarily perpendicular to the magnetic field in the inhomogeneous plasma conditions of the Earth's magnetosphere. Of particular importance is the evolution of the wave vector \mathbf{k} as the wave propagates from where the waves are generated to where the waves are ultimately damped. The propagation of waves in an inhomogeneous medium is governed by the ray equations (Weinberg, 1962)

$$\frac{d\mathbf{k}}{dt} = - \left(\frac{\partial \omega}{\partial \mathbf{x}} \right)_{\mathbf{k},t} \quad \frac{d\mathbf{x}}{dt} = \left(\frac{\partial \omega}{\partial \mathbf{k}} \right)_{\mathbf{x},t} \quad \frac{d\omega}{dt} = \left(\frac{\partial \omega}{\partial t} \right)_{\mathbf{x},\mathbf{k}} \quad (\text{A1})$$

where the linear dispersion relation for the wave gives the dependence of the wave frequency $\omega(\mathbf{k}, \mathbf{x}, t)$ on the wave vector \mathbf{k} , position \mathbf{x} , and time t .

In the limit of nearly perpendicular propagation $k_{\parallel} \ll k_{\perp}$ and small parallel wavenumber $k_{\parallel} d_i \ll 1$, the Hall MHD dispersion relation for the fast magnetosonic wave can be approximated by

$$\frac{\omega}{\Omega_i} = k d_i \sqrt{1 + \beta_i (1 + T_e/T_i)} \quad (\text{A2})$$

plotted as the dashed red line in Figure A2(a), showing that the combination of the propagating segments of the ion Bernstein modes (blue) are reasonably well approximated by this fluid linear dispersion relation for the fast magnetosonic wave. To solve the ray equations for the evolution of the normalized wave vector $\mathbf{k} d_i$ as the wave propagate from $L = 2.8$ to $L = 1.75$, we fit the magnetic field magnitude and electron density profiles over the range $1.6 \leq L \leq 3$ using

$$B(L) = M/L^3 \quad (\text{A3})$$

where $M = 30.4 \times 10^3$ nT and

$$n_e(L) = n'_e (L - L_0) + n_{e0} \quad (\text{A4})$$

With $n'_e = -1290 \text{ cm}^{-3}$, $L_0 = 1.7$, $n_{e0} = 2424 \text{ cm}^{-3}$, plotted as red lines in Figure A1.

We take the plasma parameters to be constant in time over the measurement interval we examine, so the third equation in A1 yields a constant value of ω , consistent with the observations which show the waves have constant frequency vs. L . The second ray equation governs that the wave propagates in the direction of the group velocity $\mathbf{v}_g = \partial \omega / \partial \mathbf{k}$, and for the dispersion relation (A2), the ratio of the parallel to perpendicular components of the group velocity is $v_{g,\parallel} / v_{g,\perp} = k_{\parallel} / k_{\perp} \ll 1$. Therefore, we may safely neglect the variation of the plasma parameters in direction parallel to the magnetic field (which is expected to be weak anyway), and

the first ray equation then implies that k_{\parallel} is constant as the wave propagates radially inward across the magnetic field.

The evolution of the perpendicular wavenumber vs. L can be computed by combining the ray equations to obtain

$$\frac{dk_{\perp}}{dL} = \frac{dk_{\perp}/dt}{dL/dt} = - \frac{(\partial\omega/\partial L)_{k_{\perp},t}}{(\partial\omega/\partial k_{\perp})_{L,t}} \quad (\text{A5})$$

This equation for k_{\perp} can be integrated from the proposed generation region at $L = 2.8$ down to the observed region where the waves are damped at $L = 1.75$ using the simplified models of the variation of the plasma parameters with L given in (A3) and (A4). A simpler approach, exploiting the fact that the frequency ω is constant, is to rearrange (A2) in the nearly perpendicular limit $k_{\parallel} \ll k_{\perp}$ to solve for the normalized perpendicular wavenumber $k_{\perp}d_i$ in terms of the spatially varying ion cyclotron frequency $\Omega_i(L)$ and ion plasma beta $\beta_i(L)$, giving

$$k_{\perp}d_i = \frac{\omega}{\Omega_i \sqrt{1 + \beta_i(1 + T_e/T_i)}} \quad (\text{A6})$$

The result is that the values of the normalized perpendicular wavenumbers $k_{\perp}d_i$ of each of the harmonic wave modes (indicated by green dots in Figure A2(a)) decrease by a factor of approximately 2.6 as they propagate through the inhomogeneous plasma conditions from $L = 2.8$ to $L = 1.75$.

In Figure A2(b), we plot the linear kinetic wave modes at $L = 1.75$, where the plasma parameters are $\beta_i = 0.173$, $T_i/T_e = 1$, and $v_{ti}/c = 3.3 \times 10^{-3}$. Note that at the lower β_i values closer to the Earth, the frequency gaps between the ion Bernstein modes nearly disappear, so that the Hall MHD dispersion relation (red dashed) for the fast magnetosonic wave is an even better approximation to combined propagating segments of the ion Bernstein waves. Here we have mapped each of the five harmonic wave modes to their new values of $k_{\perp}d_i$ (green dots). The plots show that ion Bernstein waves from $L = 2.8$ have mapped largely down to the fast magnetosonic mode (black dotted) when normalized to the local ion cyclotron frequency at $L = 1.75$. Therefore, we must explore the damping of the fast magnetosonic waves at this position to understand the physical mechanisms for damping these waves, as shown in Figure 4.

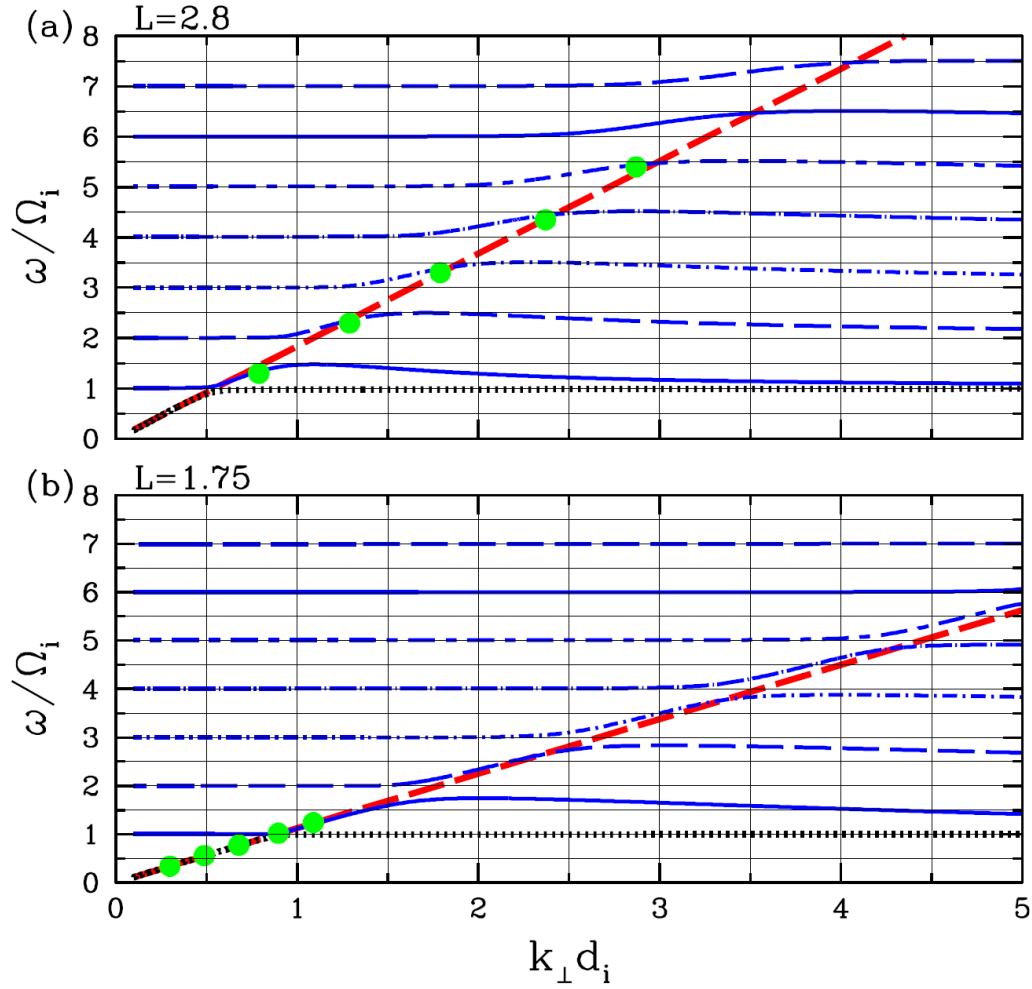


Figure A2. Linear dispersion relation for the spectrum of ion Bernstein waves (blue) and fast magnetosonic wave (black dotted) at (a) the presumed source region at $L=2.8$ and (b) the damping region at $L=1.75$. The frequency normalized to the local ion cyclotron frequency ω/Ω_i is plotted vs. the perpendicular wavenumber normalized to the local ion inertial length $k_{\perp} d_i$. The Hall MHD prediction for the fast magnetosonic wave is also plotted for comparison (red dashed). The ray equations are used to evolve the perpendicular wavenumbers in the inhomogeneous background plasma of the first five ion Bernstein modes from $L=2.8$ in panel (a) to $L=1.75$ in panel (b) (green dots).

Note that although we find that the parallel wavenumber k_{\parallel} remains constant, the normalized parallel wavenumber $k_{\parallel} d_i$ decreases because the ion inertial length changes, decreasing $k_{\parallel} d_i$ by a factor of approximately 1.5 from $L=2.8$ to $L=1.75$. Along with the decrease in $k_{\perp} d_i$ by a factor of 2.6, our findings indicate that the wave refracts as it propagates radially inward through the

inhomogeneous plasma conditions. The angle of propagation relative to the magnetic field $\theta = \tan^{-1} \left(\frac{k_{\perp}}{k_{\parallel}} \right)$ decreases with L , and this refraction has significant implications for the onset of strong wave damping at $L = 1.75$ as observed by the Van Allen Probes, as discussed in Section 4.1.

Acknowledgments

The authors thank Dr. R. S. Selesnick for reading the initial draft article and the insightful follow up discussions. The authors thank EMFISIS instrument team for pointing out the reliability of the data under certain conditions. We also thank W. S. Kurth for clarification on the data artifacts of the EMFISIS instrument during antenna shadowing. The primary author wishes to acknowledge the use of funds from NASA's Van Allen Probes ECT project, through JHU/APL contract 967399 under prime NASA contract NAS5-01072.

Data availability statement

Van Allen Probes REPT data is available from the ECT Science Operations and Data Center, https://rbsp-ect.newmexicoconsortium.org/data_pub/rbspb/rept, EMFISIS data from <http://emfisis.physics.uiowa.edu> and EFW data from <http://rbsp.space.umn.edu>.

References

- Baker, D.N., Kanekal, S.G., Hoxie, V.C., Batiste, S., Bolton, M., Li, X., Elkington, S. R. *et al.* (2013), The Relativistic Electron-Proton Telescope (REPT) Instrument on Board the Radiation Belt Storm Probes (RBSP) Spacecraft: Characterization of Earth's Radiation Belt High-Energy Particle Populations. *Space Sci Rev*, 179, 337–381. doi:10.1007/s11214-012-9950-9
- Boardsen, S. A., Gallagher, D. L., Gurnett, D. A., Peterson, W. K., & Green, J. L. (1992). Funnel-shaped, low-frequency equatorial waves. *Journal of Geophysical Research*, 97, 14,967–14,976.

Cairns R. A., (1985), '*Plasma Physics*', Blackie, Glasgow, Scotland. DOI: 10.1007/978-94-010-9655-3

Dragt, A. J., Austin, M. M., & White, R. S. (1966). Cosmic ray and solar proton albedo neutron decay injection. *Journal of Geophysical Research*, 71(5), 1293–1304, doi:10.1029/JZ071i005p01293

Gary, S. P., Liu, K., Winske, D., and Denton, R. E. (2010). Ion Bernstein instability in the terrestrial magnetosphere: Linear dispersion theory. *Journal of Geophysical Research*, 115(A12):A12209.

Gurnett, D. A. (1976), Plasma wave interactions with energetic ions near the magnetic equator, *J. Geophys. Res.*, 81(16), 2765–2770, doi:10.1029/JA081i016p02765.

Gussenhoven, M.S., Mullen, E.G., Violet, M.D., Hein, C., Bass, J., and Madden, D. (1993), CRRES High Energy Proton Flux Maps, *IEEE Transactions on Nuclear Science*, Vol. 40, No. 6, doi: 10.1109/23.273519

Hartley, D. P., Kletzing, C. A., De Pascuale, S., Kurth, W. S., & Santolík, O. (2018), Determining plasmaspheric densities from observations of plasmaspheric hiss, *Journal of Geophysical Research: Space Physics*, 123, 6679–6691. doi:10.1029/2018JA025658.

Horne, R. B., Wheeler, G. V., & Alleyne, H. S. C. K. (2000). Proton and electron heating by radially propagating fast magnetosonic waves. *Journal of Geophysical Research*, **105**(A12), 27,597– 27,610. Doi:10.1029/2000JA000018.

Horne, R. B., Thorne, R. M., Chen, L., Tao2, X., Jordanova, V. K., Pokhotelov, D. and Robert, P., (2011), Ion heating by fast magnetosonic waves and ring current-electron radiation belt coupling Abstract #SM21C-04, *presented at 2011 Fall Meeting*, AGU, San Francisco, Calif.

Horne, R. B., and Miyoshi, Y. (2016), Propagation and linear mode conversion of magnetosonic and electromagnetic ion cyclotron waves in the radiation belts, *Geophys. Res. Lett.*, 43, 10,034–10,039, doi:10.1002/2016GL070216.

Hrbáčková, Z., Santolík, O., Němec, F., Macůšová, E. and Cornilleau-Wehrlin, N., (2015), Systematic analysis of occurrence of equatorial noise emissions using 10 years of data from the Cluster mission, *J. Geophys. Res. Space Physics*, 120, 1007–1021, doi:10.1002/2014JA020268.

Hudson, M. K., Kotelnikov, A. D., Li, X., Roth, I., Temerin, M., Wygant, J., Blake, J. B., & Gussenhoven, M. S. (1995). Simulation of proton radiation belt formation during the March 24, 1991 SSC. *Geophysical Research Letters*, 22(3), 291–294, doi:10.1029/95GL00009

Klein, K. G. and Howes, G. G. (2015). Predicted impacts of proton temperature anisotropy on solar wind turbulence. *Physics of Plasmas*, 22(3):032903.

Kletzing, C. A., Kurth, W. S., Acuna, M., MacDowall, R. J., Torbert, R. B., Averkamp, T., et al. (2013). The electric and magnetic field instrument suite and integrated science (EMFISIS) on RBSP. *Space Science Reviews*, 179(1–4), 127–181. doi:10.1007/s11214-013-9993-6.

Li, X., Xiang, Z., Zhang, K., Khoo, L., Zhao, H., Baker, D. N., & Temerin, M. A. (2020). New Insights From Long-Term Measurements of Inner Belt Protons (10s of MeV) by SAMPEX, POES, Van Allen Probes, and Simulation Results. *Journal of geophysical research. Space physics*, 125(8), doi:10.1029/2020JA028198

Looper, M. D., Blake, J. B., & Mewaldt, R. A. (2005). Response of the inner radiation belt to the violent Sun-Earth connection of October–November 2003. *Geophysical Research Letters*, 32, L03S06, doi:10.1029/2004GL021502

Lorentzen, K. R., Mazur, J. E., Looper, M. D., Fennell, J. F., & Blake, J. B. (2002). Multisatellite observations of MeV ion injections during storms. *Journal of Geophysical Research*, 107(A9), 1231, doi:10.1029/2001JA000276

- Ma, Q., Li, W., Thorne, R. M. and Angelopoulos, V., (2013), Global distribution of equatorial magnetosonic waves observed by THEMIS, *Geophys. Res. Lett.*, **40**, 1895– 1901, doi:10.1002/grl.50434.
- Ma, Q., Li, W., Bortnik, J., Kletzing, C. A., Kurth, W. S., Hospodarsky, G. B., & Wygant, J. R. (2019). Global survey and empirical model of fast magnetosonic waves over their full frequency range in earth's inner magnetosphere. *Journal of Geophysical Research: Space Physics*, 124, 10270– 10282, doi:10.1029/2019JA027407.
- Nemec, F., O. Santolík, K. Gereova, E. Macusova, Y. de Conchy, and N. Cornilleau-Wehrlin (2005), Initial results of a survey of equatorial noise emissions observed by the Cluster spacecraft, *Planet. Space Sci.*, **53**, 291– 298.
- Russell, C. T., and Holzer, R. E., (1970), OGO 3 observation of ELF noise in the magnetosphere 2. The nature of the equatorial noise, *J. Geophys. Res.*, 75(4), 755–768, doi:10.1029/JA075i004p00755.
- Santolík, O., Pickett, J. S., Gurnett, D. A., Maksimovic, M., Cornilleau-Wehrlin, N., (2002), Spatiotemporal variability and propagation of equatorial noise observed by Cluster, *J. Geophys. Res. Space Physics*, 107, A12 doi:10.1029/2001JA009159.
- Santolík, O., Parrot, M., and Lefeuvre, F., (2003), Singular value decomposition methods for wave propagation analysis, *Radio Sci.*, 38(1), 1010, doi:10.1029/2000RS002523.
- Santolík, O., Nemec, F., Gereová, K., Macúšová, E., de Conchy, Y., & Cornilleau-Wehrlin, N. (2004). Systematic analysis of equatorial noise ~ below the lower hybrid frequency. *Annals of Geophysics*, 22, 2587–2595.
- Sawyer, D.M., Vette, J.I. (1976), AP-8 trapped proton environment for solar maximum and solar minimum, NASA WDC-A-R&S 76-06, NASA-TM-X-72605

- Selesnick, R. S., Looper, M. D., & Mewaldt, R. A. (2007). A theoretical model of the inner proton radiation belt. *Space Weather*, 5, S04003, doi:10.1029/2006SW000275
- Selesnick, R. S., Baker, D. N., Jaynes, A. N., Li, X., Kanekal, S. G., Hudson, M. K. and Kress, B. T., (2014), Observations of the inner radiation belt: CRAND and trapped solar protons, *J. Geophys. Res. Space Physics*, 119, 6541–6552, doi:10.1002/2014JA020188.
- Selesnick, R. S., Baker, D. N., Kanekal, S. G., Hoxie, V. C., & Li, X.(2018). Modeling the proton radiation belt with Van Allen Probes Relativistic Electron-Proton Telescope data. *Journal of Geophysical Research: Space Physics*, 123, 685–697, doi:10.1002/2017JA024661
- Selesnick, R. S., & Albert, J. M. (2019). Variability of the proton radiation belt. *Journal of Geophysical Research: Space Physics*, 124, 5516–5527, doi:10.1029/2019JA026754
- Singer, S. F. (1958). “Radiation belt” and trapped cosmic-ray albedo. *Physical Review Letters*, 1(5), 171–173, doi:10.1103/PhysRevLett.1.171
- Somov B.V. (2013), Wave-Particle Interaction in Astrophysical Plasma. In: *Plasma Astrophysics, Part I*. Astrophysics and Space Science Library, vol 391. Springer, New York, NY, doi:10.1007/978-1-4614-4283-7_7
- Stasiewicz, K. (1993), Finite Larmor Radius Effects in the Magnetosphere, *Space Science Reviews*, Volume 65, Issue 3-4, pp. 221-252, doi: 10.1007/BF00754509
- Stix T. H. (1990), Waves in plasmas: Highlights from the past and present, *Physics of Fluids B: Plasma Physics* 2, 1729, doi:10.1063/1.859444.
- Vette, J.I. (1966), Models of the Trapped Radiation Environment, Vol. I: Inner Zone Protons and Electrons, NASA SP-3024.

Weinberg, S. (1962). Eikonal Method in Magnetohydrodynamics. *Physical Review*,
126(6):1899–1909.

Wygant, J. R., Bonnell, J.W., Goetz, K., Ergun, R.E., Mozer, F.S., Bale, S.D., Ludlamet, M., et
al. (2013), The electric field and waves instruments on the radiation belt storm probes mission,
Space Sci. Rev., 179(1–4), 183–220, doi:10.1007/s11214-013-0013-7.